Check for updates

Tunable, Grating-Gated, Graphene-On-Polyimide Terahertz Modulators

Alessandra Di Gaspare, Eva Arianna Aurelia Pogna, Luca Salemi, Osman Balci, Alisson Ronieri Cadore, Sachin Maruti Shinde, Lianhe Li, Cinzia di Franco, Alexander Giles Davies, Edmund Harold Linfield, Andrea Carlo Ferrari, Gaetano Scamarcio, and Miriam Serena Vitiello*

An electrically switchable graphene terahertz (THz) modulator with a tunable-by-design optical bandwidth is presented and it is exploited to compensate the cavity dispersion of a quantum cascade laser (QCL). Electrostatic gating is achieved by a metal grating used as a gate electrode, with an HfO_2/AlO_x gate dielectric on top. This is patterned on a polyimide layer, which acts as a quarter wave resonance cavity, coupled with an Au reflector underneath. The authors achieve 90% modulation depth of the intensity, combined with a 20 kHz electrical bandwidth in the 1.9–2.7 THz range. The modulator is then integrated with a multimode THz QCL. By adjusting the modulator operational bandwidth, the authors demonstrate that the graphene modulator can partially compensate the QCL cavity dispersion, resulting in an integrated laser behaving as a stable frequency comb over 35% of the operational range, with 98 equidistant optical modes and a spectral coverage ~1.2 THz. This paves the way for applications in the terahertz, such as tunable transformation-optics devices, active photonic components, adaptive and quantum optics, and metrological tools for spectroscopy at THz frequencies.

Dr. A. Di Gaspare, Dr. E. A. A. Pogna, L. Salemi, Prof. M. S. Vitiello
NEST
CNR-NANO and Scuola Normale Superiore
Pisa 56127, Italy
E-mail: miriam.vitiello@sns.it
Dr. O. Balci, Dr. A. R. Cadore, Dr. S. M. Shinde, Prof. A. C. Ferrari
Cambridge Graphene Centre
Cambridge CB3 0FA, UK
Dr. L. Li, Prof. A. G. Davies, Prof. E. H. Linfield
School of Electronic and Electrical Engineering
University of Leeds
Leeds LS2 9JT, UK
C. di Franco, Prof. G. Scamarcio
CNR-IFN and Dipartimento Interateneo di Fisica
Università degli Studi di Bari
Bari I-70126, Italy

The ORCID identification number(s) for the author(s) of this article can be found under https://doi.org/10.1002/adfm.202008039.

1. Introduction

Key photonic applications in the far-infrared, i.e., 1–10 THz frequencies, require modulation and switching of the optical signals with high speeds (electronic bandwidth > 10 kHz), large (>50%) amplitude modulation (AM) depths, and frequency tuning.[1] E.g., high-throughput wireless transmission over short-range links requires an efficient (>50%) intensity modulation,[2] fast (<µs) spatial light modulation is desirable for high-resolution imaging,[3] and spectroscopy systems, THz communications rely on the development of fast reconfigurable components for amplitude, frequency, and phase stabilization.[4,5] The 0.1–10 THz range is interesting for future high speed communications, since the high carrier frequencies would allow unprecedented channel capacities. E.g., ref. [2] reported single-input and single-output wireless communication systems at 0.2375 THz for transmitting data over 20 m, at a data rate ~100 Gbit s⁻¹.

Miniaturized quantum cascade laser (QCL) sources, operating at THz frequencies[6,7] can support very high modulation rates (up to tens of GHz)[8,9] through direct modulation of their operating current.[10,11] However, they require cryogenic[7] or Peltier cooling.[12–14] The modulation of their driving current often induces undesired effects, such as current instabilities,[6,7] or a simultaneous amplitude and frequency self-modulation.[15] Hence, the need to use small cavities with low (µW) power outputs, with major drawbacks for applications. Thus, electro–optical modulators independent from source-detector combination, or integrated with a specific source, are highly desirable.

Single layer graphene (SLG) with its broadband and electrically tunable optical conductivity[16] is an ideal platform for the development of electrically switchable electro–optic modulators.[17–19] The optical conductivity of SLG is defined by the interband and intraband electronic transitions between, or within, the conduction band (CB) and valance band.[17,20] In the visible, near-infrared, and mid-infrared, interband transitions dominate the optical conductivity of SLG.[20,21] In intrinsic SLG, the light absorption in the IR and visible is ~$\pi\alpha$ ~2.3%, where α is the fine structure constant.[21] By shifting the chemical potential

**ADVANCED
SCIENCE NEWS**
www.advancedsciencenews.com

**ADVANCED
FUNCTIONAL
MATERIALS**
www.afm-journal.de

below or above the half frequency of impinging radiation via electrostatic gating, the absorption can be tuned, thanks to Pauli blocking.[19] High modulation amplitudes can then be achieved by employing multiple SLGs.[17,22] At THz frequencies, however, interband transitions are usually blocked due to the fact that as-prepared SLG is doped,[23,24] hence intraband electronic transitions dominate the optical conductivity.[25] Consequently, SLG behaves as a 2D electron gas and has a Drude-like conductivity in the form of $\sigma = iD/\pi(\omega + i\Gamma)$, where ω is the light frequency, Γ is the scattering rate, $D = (v_F e^2 / \hbar)\sqrt{\pi |n|}$ with v_F the Fermi velocity, n the charge carrier density.[26–28] This can be controlled by means of either electrostatic gating[28] or optical excitation[25] over a spectral range significantly broader compared to conventional semiconductors.[29] Tuning σ enables control of the light-SLG interactions by means of transmission, reflection, and absorption.[17,19] For free standing SLG, higher σ results in higher reflection and lower transmission of THz-frequency light, and the absorption reaches its maximum when the sheet resistance (R_s) of SLG reaches half of the free space impedance ($Z_0 = 377\ \Omega$).[30]

The progress in the large area growth and transfer of SLG[23,31] has enabled the development of SLG-based active devices such as modulators,[18] absorbers,[32] phase shifters,[5] and reflect-arrays[33] at THz frequencies.[34–36] In all these devices, phase and amplitude control of the incident light were achieved by tuning the SLG charge density by all-electronic[37,38] or all-optical[39,40] architectures. A variety of configurations were used to design SLG-THz reflection modulators. These include: architectures based on SiO$_2$/undoped Si, with an Au reflector on the back and a ring-shaped electrode on the SLG,[37] in which the charge density of SLG was tuned via the back-gate, achieving amplitude modulation (AM) between 15% and 64% at 20 kHz speed between 0.59 and 0.63 THz;[37] modulators relying on plasmonic metamaterials, exhibiting narrow (<100 GHz) bandwidths, large modulation depths (>50%) enabled by the field enhancement, and switching speeds >10 MHz in the sub-THz range;[41] configurations exploiting the change in conductivity of multilayer graphene to externally modulate the LC plasmonic resonance of a periodic pattern of metallic meta-atoms externally,[42] achieving 58% AM, phase modulation of 65° and a 12 MHz speed at 0.8 THz; split-ring resonators strongly coupled to SLG surface plasmons,[43] allowing 60% modulation at a fixed and very sharp frequency (4.7 THz) with 40 MHz speeds; Brewster angle devices[44] and chiral metamaterials,[45,46] all operating at frequencies <1.5 THz, and many other schemes.[47,48]

However the combination of high modulation efficiencies (>60%) and modulation speeds <100 µs, with tunable and broadband operation, in a miniaturized (<0.2 mm) configuration that can be integrated easily, and at frequencies >2 THz, was not achieved to date, to the best of our knowledge.

Here, we present a SLG-based THz modulator with a tunable-by-design optical bandwidth. The electrostatic gating of SLG is achieved by a grating coupler, used as a gate electrode, and covered by HfO$_2$/AlO$_x$. This is patterned on a polyimide layer that acts as a quarter wave resonance cavity together with an Au reflector underneath. We achieve large modulation depths (90%) and ≥20 kHz electrical bandwidth, in the 1.9–2.7 THz range. We then integrate our device on-chip, with

miniaturized THz QCL sources to alter the oscillating phase of the reflected intracavity field.

QCLs can inherently operate as frequency combs (FCs) both in the mid-infrared[49] and THz[50–54] through four-wave-mixing (FWM), spontaneously arising in the laser cavity as a consequence of the strong third-order non-linear susceptibility of the gain medium.[52] However, at THz frequencies, this only happens spontaneously over a restricted operational range (<23%),[50–54] in which the group delay dispersion (GDD) is compensated. Alleviating this, by engineering and compensating the cavity dispersion over the entire dynamic range, is a demanding task, since semiconductor materials are highly dispersive at THz frequencies. Current methods to achieve this rely on Gires–Tournois interferometer (GTI)[55] schemes, with a biased,[56] or amplitude frequency-modulated, section,[57], or on tightly coupled passive external cavity architectures,[58,59] allowing limited power outputs,[57] or a limited increase of the dispersion compensated regime.[58,59]

Here, we demonstrate that the integration of SLG modulators with THz QCLs results in phase-locking of the laser modes, in an operational regime in which it cannot occur spontaneously, due to the inherent intracavity GDD. The integrated system behaves as a frequency comb, spontaneously, over 35% of the laser operational range, thereby opening perspectives for tunable high-resolution spectroscopy and quantum metrology.

2. Results and Discussion

2.1. Modulator Design

The design of the modulator, operating in reflection mode, is schematically shown in **Figure 1**a. To fabricate the device, we first deposit a 14 µm thick polyimide layer as a dielectric spacer (permittivity, $\varepsilon_{poly} = 3.5$ in the 2–4 THz range) on an Au/SiO$_2$/Si substrate (see Experimental Section). The polyimide thickness is chosen to match the $\lambda/4$ waveguide mode at the central frequency $\nu = 2.85$ THz of our multimode QCL. Then, we prepare a SLG capacitor on the polyimide layer as the active component of the device, as shown in Figure 1a (see Experimental Section). The metal grating with a period p couples with the quarter wave mode and defines the modulator resonant frequency, while acting as the counter electrode of the SLG capacitor (see Experimental Section).

To understand the optical characteristics of our devices, we perform finite element simulations with COMSOL Multi-Physics, using the Wave Optics Module. We model all the metal layers as perfect electrical conductor boundaries, and use Floquet periodic boundary condition, to create the metal grating. The optical constants of polyimide (Kapton) in the THz range are taken from ref. [60]. We use $\varepsilon_1 = 20$, thickness $t_1 = 40$ nm for HfO$_2$, and $\varepsilon_2 = 9$, thickness $t_2 = 100$ nm for AlO$_x$. We model SLG as a transient boundary condition with a Drude-like complex conductivity, and a Fermi energy (E_F) dependent scattering time. We then calculate the spatial electric field (E-field) distribution of incident THz light with a polarization perpendicular to the grating at 2.48 THz. Figure 1b shows that the E-field intensity is mostly focused at the grating edges. We also calculate the E-field distribution in the incident light direction,
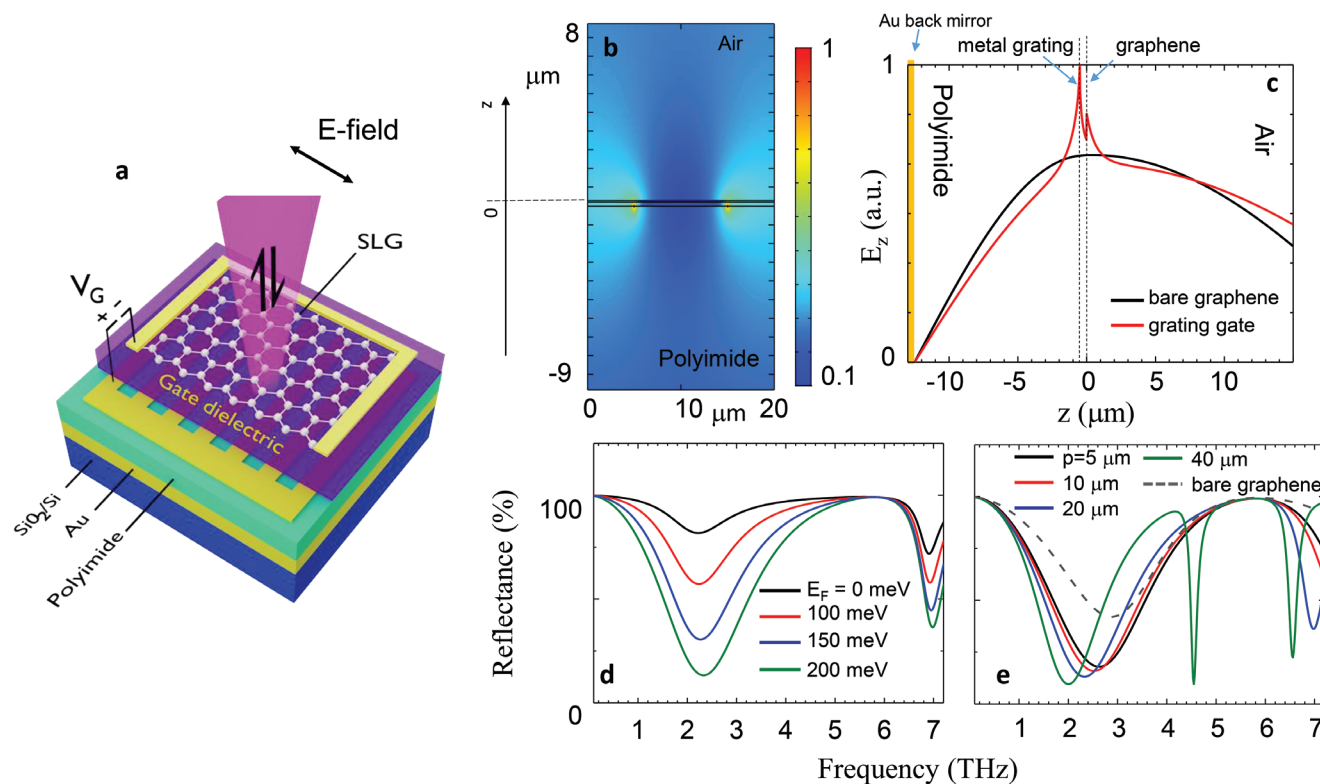
**ADVANCED
SCIENCE NEWS**
www.advancedsciencenews.com

**ADVANCED
FUNCTIONAL
MATERIALS**
www.afm-journal.de

Figure 1. Grating-gated SLG THz modulator design. a) Schematic of modulator layout under top illumination, comprising a metal grating-SLG capacitor patterned on polyimide on Au. b) Spatial distribution of the optical electric field on the metal grating-SLG capacitor, calculated for $p = 20$ μm (metal width 10 μm) at the quarter wave resonance at $f = 2.48$ THz. c) Electric-field intensity profile along the direction of incidence for SLG (black) at 3 THz and for grating-gated SLG (red) at 2.48 THz on polyimide. d) Calculated reflectance of grating-gated SLG modulator for different SLG E_F for $p = 20$ μm. To calculate the modulator reflectance at $E_F = 0$ meV, the SLG conductivity is set to the universal conductivity value $\sigma_0 = 6.08 \times 10^{-5}$ S.[26] The grating mode is ~6.88 THz. e) Calculated reflectance for SLG (dashed line) and grating-gated SLG THz modulators with different p (continuous lines).

Figure 1c, for SLG on polyimide and Au reflector at 3 THz, and for grating-gated SLG at 2.48 THz, i.e., at the related $\lambda/4$ mode resonance frequencies. The intensity becomes zero on the Au reflector, because of the discontinuity of E-field on a perfect conductor, and is maximum on the grating and SLG surfaces, because of the quarter wave resonance. To simulate the reflected THz intensity modulation as a function of SLG E_F, we first calculate the fringing direct current (DC) E-field from the grating gate electrode using the alternative current (AC)/DC module in COMSOL (see Supporting Information). The fringing field extends up to ~2.5 μm at the edge of the grating gate, as a consequence of the finite impedance of the gate dielectric. We use the calculated field profile to shift E_F of SLG on top and on each side of the grating gate. We simulate the reflectance of the grating-gated SLG THz modulator with $p = 20$ μm, Figure 1d, and for a set of different grating periodicities (Figure 1e).

The reflected light intensity decreases as E_F increases, because of the increasing intraband absorption of SLG.[17,20,37] Then, we consider the reflectance for different grating periods after setting $|E_F|$ ~200 meV, as estimated from Raman spectroscopy (see Supporting Information). The quarter wave mode of SLG couples with the grating mode and shifts toward lower frequencies as the grating pitch increases from 5 to 40 μm, Figure 1e. By choosing the pitch size, we set the modulator spectral band in the 2–4 THz range, simultaneously keeping the grating mode outside this

range, as seen by the narrow resonance appearing at 4.53 THz for $p = 40$ μm (green curve in Figure 1e), corresponding to the first-order photonic mode of the grating gate cavity. This ensures a narrower band and a higher spectral tunability, when compared to the quarter wave resonance mode of SLG, whose linewidth is set by the polyimide thickness. A strong (>50%) reflectance modulation of incident THz light can be achieved by tuning E_F by electrostatic gating, after engineering the grating gate to move the quarter wave resonance to the targeted frequency.

2.2. Performance of Graphene Terahertz Modulators

We measure the performance of our grating-gated SLG modulators using a THz time domain spectroscopy (TDS) system (Menlo Terasmart k5) in reflection (see Experimental Section and Supporting Information). The time-domain THz signal is acquired with a delayed-pulse sampling window of 70 ps, resulting in a spectral resolution ~15 GHz. The beam spot diameter in reflection is 1.5 mm, i.e., smaller than the active area of the modulators (~2.5 × 4 mm²). We measure the reflectance of SLG modulators with p ranging from 5 to 45 μm at different gate voltages.

The time-domain traces (**Figure 2**a–d) reveal that the quarter wave resonance shifts from ~1.9 to ~2.9 THz as p changes from

**ADVANCED
SCIENCE NEWS**

www.advancedsciencenews.com

**ADVANCED
FUNCTIONAL
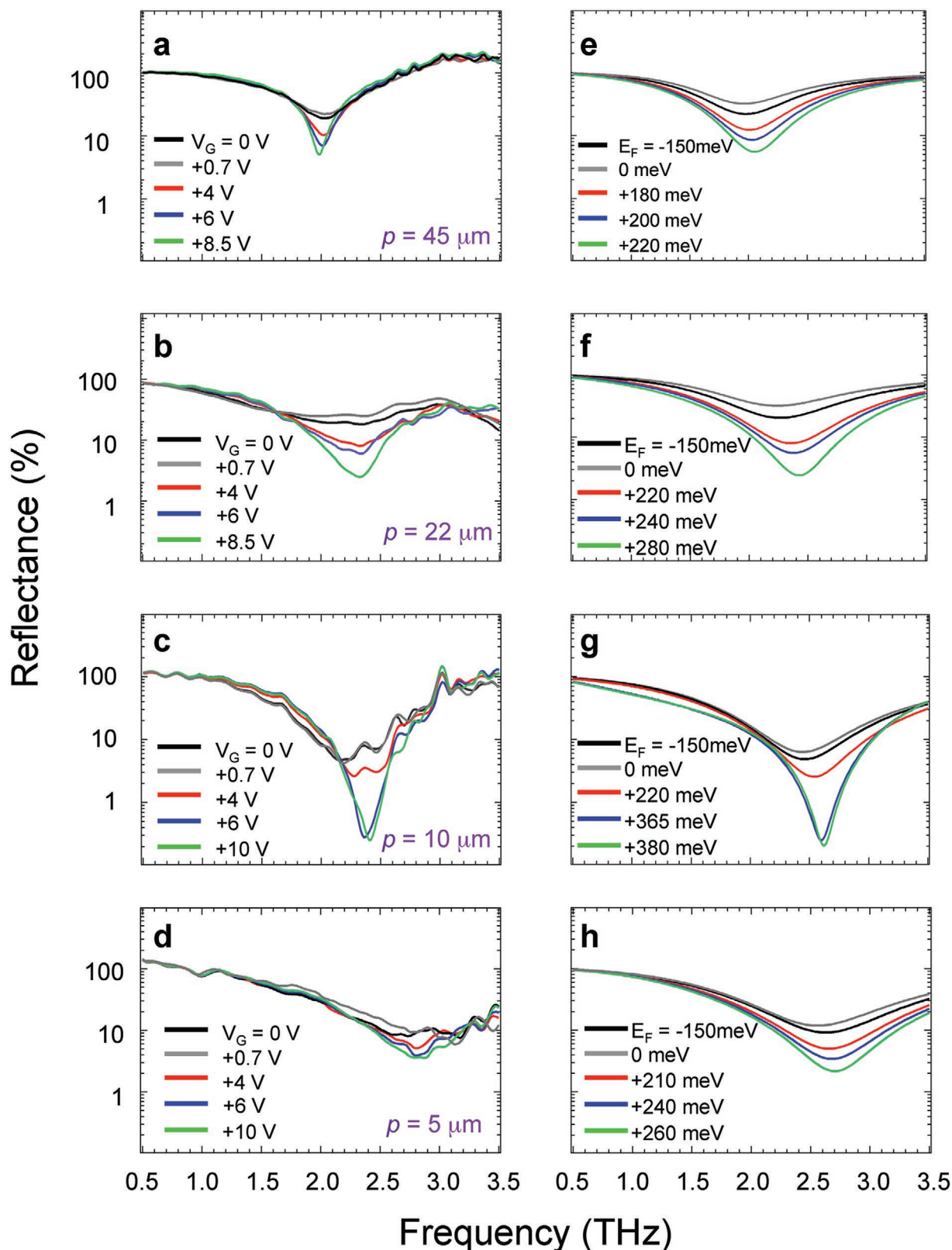MATERIALS**

www.afm-journal.de

Figure 2. TDS Reflectance spectra: a–d). Total reflectance as a function of V_G using a time-domain spectroscopy system for four modulators having different $p = 45$ µm (a), 22 µm (b), 10 µm (c), and 5 µm (d); e–h) Calculated total reflectance for the same p of panels (a–d) at different E_F. In the simulated curves, the E_F chosen to reproduce the experimental data are in agreement with a conductivity tuning corresponding to the experimental V_G, by assuming $n_0 \sim 1.45 \times 10^{12}$ cm^{-2} for $p = 22$, 45 µm, $n_0 \sim 3.70 \times 10^{12}$ cm^{-2} for $p = 10$, and $n_0 \sim 3.35 \times 10^{12}$ cm^{-2} for $p = 5$ µm. The sign of E_F is conventionally negative for p-type doping ($V_G < V_{CNP}$), and positive for n-type doping ($V_G > V_{CNP}$). In our sample, $V_{CNP} = +0.7$ V, as revealed by the IV measurements of the SLG FET (see Supporting Information), and the SLG is initially p-doped with $|E_F| \sim 200$ meV.

45 to 5 µm, with the same polyimide thickness ~14 µm. The reflectance from the modulators slightly increases as the gate voltage, V_G, changes from 0 to V_{CNP} = +0.7 V. It then decreases at $V_G > V_{CNP}$, due to the increasing charge density on SLG. V_{CNP} is defined as V_G at the charge neutrality point (CNP), (see Supporting Information). V_G is applied to the grating electrode. $V_G > V_{CNP}$ shifts E_F in the CB upward and accumulates electrons on SLG. The intraband transition rate gets higher with larger charge density, and the quarter wave resonance becomes deeper, due to the increasing intraband absorption of SLG.[17,19,37]

We simulate the optical performance of our SLG modulators using COMSOL MultiPhysics (see Experimental Section and Supporting Information) for the same device configurations as those experimentally measured. We enter SLG E_F, mobility, and residual charge density, n_0, in its Drude-like intraband conductivity to reproduce the experimentally measured reflectance. The E_F dependent scattering time, $\tau = \mu E_F / e v_F$, where μ is the mobility, e is the electron charge, and v_F is the Fermi velocity, is then calculated by setting $\mu \approx 1600$ cm² V⁻¹ s⁻¹ as measured from the electron transport characteristics of a field effect transistor (FET) (see Supporting Information).

The calculated reflectances (Figure 1e, Figure 2e–h) are in agreement with experiments (Figure 2a–d). The E_F values in Figure 2e–h are compatible with those expected from the SLG electrostatic gating, assuming $n_0 \sim 1.40$–3.70×10^{12} cm⁻² and a gate capacitance $C_G = 65$ nF cm⁻² (see Supporting Information). The corresponding conductivities match the values expected from the electrostatic gating of a SLG FET having the same gate

capacitance of our modulator. The initial doping is that directly measured by Raman spectroscopy and the graphene FET IV characteristics. This n_0, due to the background free carrier density, gives a gate-independent contribution to the total reflectance at $V_G = V_{CNP}$. The highest doping is for modulators with the smaller grating pitches (5,10 µm), where the density of the grating edges is higher. These may increase the doping due to charge transfer.[61]

Although we can reproduce the modulation of the reflected THz light from each device, the expected crossing of the Dirac point and increase of the reflectance for negative V_G is not seen. We attribute this to doping-inhomogeneity over the large 2.5×4 mm² area of the modulator, which prevents the homogeneous p-type carriers' accumulation below the CNP.

To evaluate the modulation performances, we extract the modulation depth defined as: $\eta = 100 \times \left(\dfrac{R(V_G) - R(V_{CNP})}{R(V_{CNP})} \right)$, where $R(V_G)$ is the reflectance extracted by the TDS data at V_G, and $R(V_{CNP})$ is the maximum reflectance, measured at $V_G = V_{CNP}$. This figure of merit is a close estimate of the modulation depth, accounting for the reflectance variation relative to the Dirac voltage. For $p = 10$ µm, and $V_G = +10$ V, η reaches a maximum ~90% (**Figure 3**a). The corresponding insertion loss, defined as the ratio between the power reflected form the modulator and that reflected from an ideal Au mirror (R = 100%) calculated over the modulator optical bandwidth, is ~1.3 dB, in agreement with the expected THz optical losses of SLG for $E_F \sim -200$ meV (see Supporting Information).

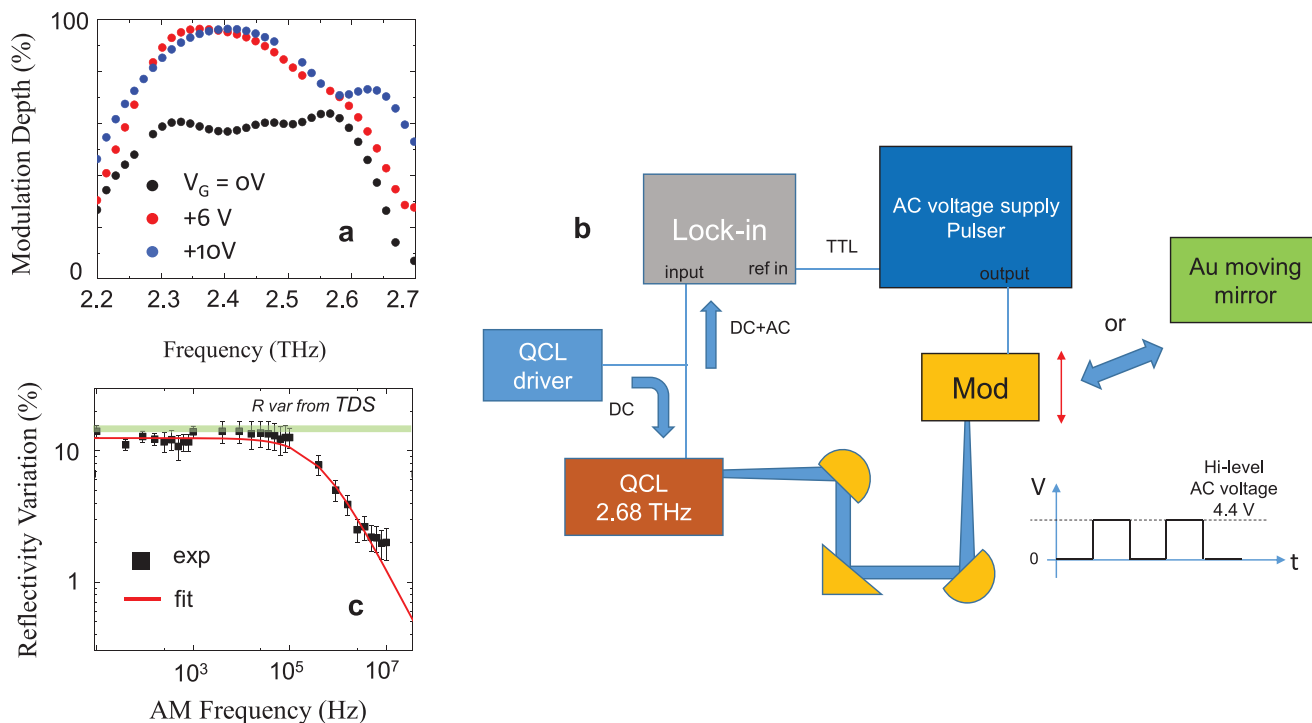**Figure 3.** Modulator performances. a) Modulation depth calculated for $p = 10$ µm and resonance frequency 2.45 THz, with $V_{CNP} = 0.7$ V. b) Schematic set-up to measure the modulation speed. The modulator is at the focal point of an external cavity comprising a single-plasmon CW QCL with single mode emission at 2.68 THz. The SM signal as a function of the frequency of the signal driving the modulator is recorded using a lock-in amplifier. The same configuration is used to acquire the reference SM signal, employing a moving Au mirror. The Au mirror is mounted on an AC-voltage-controlled piezoelectric stage, moving along the direction indicated by the red arrow. c) Modulation speed, estimated through the reflectance variation (ΔR), extracted from the QCL self-mixing signal as a function of the driving amplitude modulation speed in the set-up shown in (b).

**ADVANCED
SCIENCE NEWS**
www.advancedsciencenews.com

**ADVANCED
FUNCTIONAL
MATERIALS**
www.afm-journal.de

To measure the modulation speed, the modulator is placed at the focal point of an external cavity comprising a single-plasmon QCL which operates continuous wave (CW), with single mode emission at 2.68 THz. The single mode signal as a function of the frequency driving the modulator is recorded by a lock-in amplifier. The same configuration is used to acquire the reference modulation speed, employing a moving Au mirror, mounted on an AC-voltage-controlled piezoelectric stage moving along the direction indicated by the arrow in Figure 3b.

The modulation speed (Figure 3c) is then assessed through a detectorless approach exploiting self-mixing interferometry,[62–64] i.e., by measuring the voltage change across the electrical contacts of a QCL operating at 2.7 THz, by employing the arrangement in Figure 3b. The physical principle is the intracavity reinjection of a small fraction (10^{-4}–10^{-2}) of the emitted field that coherently interferes within the QCL cavity. In Figure 3b, the modulator acts as back mirror of an external cavity QCL. We therefore retrieve the down-converted signal arising from the E-field back-reflected by the modulator, which behaves as a gate-controlled active mirror of the external cavity QCL. The self-mixing trace then captures the reflectance variation corresponding to the applied AC gate voltage, hence the maximum modulation speed achievable while changing the AM frequency of the AC voltage.

We extrapolate the reflectance variation corresponding to the high- (+4.4 V) and low- (0 V) levels of the applied AC gate voltage from the TDS data. At the operating frequency of the QCL, such variation is ~15%, very close to the flat-region value of the measured self-mixing signal at low ($<10^3$ Hz) frequencies (Figure 3c). The 3 dB cutoff frequency extrapolated from the fit, $f_{c.o,fit.} = 19.5 \pm 1.8$ kHz, is in good agreement with the theoretical electronic cutoff $f_{c.o,teo} = 24.5$ kHz, obtained by approximating the modulator with an equivalent low-pass RC circuit having $R = 1$ kΩ (the SLG resistance, measured directly on the sample with a two-probe method) and $C = 6.5$ nF, the overall modulator capacitance. The latter is calculated as $C = C_G \times A_{mod}$, where $A_{mod} = 10$ mm² is the total modulator area, and C_G is obtained as the series of the capacitances of the two dielectric layers: HfO_2 ($\varepsilon_1 = 20$, thickness $t_1 = 40$ nm, $C_1 = 450$ nF cm⁻²), and AlO_x ($\varepsilon_2 = 9$, $t_2 = 100$ nm, $C_2 = 76$ nF cm⁻²). The measured speed (50 µs) arises from a combination of device size and optimization of optical coupling. Thus, our design has the potential to achieve MHz modulation bandwidths, by combining device scaling and optical coupling optimization, e.g., by reducing the modulator area to that of the facet of a THz QCL microlaser (15 µm × 85 µm), the gate capacitance would decrease by ~4 orders of magnitude, meaning that, even if the SLG resistance is partially affected by the more rectangular geometry, the modulator electrical bandwidth could reach 40 MHz.

2.3. Integration of Single Layer Graphene-Terahertz Modulator with a Quantum Cascade Laser-Gires–Tournois Interferometer

We then investigate the performance enhancement induced by our SLG modulators on the intracavity mode dynamics of a heterogeneous multimode THz QCL, by coupling a SLG modulator with a QCL. The QCL comprises a 17-µm-thick GaAs/AlGaAs heterogeneous heterostructure, featuring a sequence of three active region modules with frequency-detuned gain bandwidths[54] centered at 2.5, 3, and 3.5 THz.[65] The Fabry–Pérot device operates as frequency comb synthesizer over ~1.05 THz bandwidth, and shows a stable and narrow (4.15 kHz) beatnote over a continuous current range ~106 mA, corresponding to 15% of the laser operational range. Different to previous approaches,[66] we then engineer an etalon-like interferometric scheme, in which the modulator is tightly coupled to the back facet of the THz QCL, at a distance ~50 µm, as required for an on-resonance GTI.[58] The THz radiation is injected in the laser cavity after being back-reflected by the modulator, operating as the external cavity active mirror of a GTI. The motivation is to exploit the comb sensitivity to the optical feedback in the modulator-GTI configuration, to achieve partial compensation of the GDD in the QCL cavity. The reflectivity spectrum and the employed resonant architecture, in the explored frequency range, minimize the total cavity dispersion, since the phase of the reflected light and, therefore, the GDD, oscillates according to the predefined modulator resonance. To verify this, we calculate the GDD for the QCL-modulator coupled system for $p = 5$, 10, 22 µm, chosen to cover three configurations: i) when the modulator optical bandwidth is superimposed with the QCL gain bandwidth ($p = 5$ µm); ii) when it is shifted towards the low-frequency side of the laser bandwidth ($p = 10$ µm); iii) when it is completely detuned ($p = 22$ µm).

The calculated GDD curves in **Figure 4** are obtained from the sum of the individual contributions arising from the GTI-QCL and from the modulator only (see Experimental Section). The antisymmetric profile of the modulator GDD comprises a low frequency negative region, which changes sign toward higher frequencies. The zero-crossing point corresponds to the measured absorption resonance. The GDD amplitude increases while varying E_F. In the coupled system, the total GDD is reduced in the low-frequency region of the QCL gain bandwidth (~2.2–2.7 THz), particularly for $p = 5$ µm (Figure 4a) and 10 µm (Figure 4b).

In the investigated p range, the integration of the modulator is expected to have a detrimental effect at frequencies >2.7 THz, especially for larger $p = 22$ µm (Figure 4c) and mismatched QCL/modulator bandwidths. As a general trend, the GDD amplitude increases for larger p, due to the higher optical strength and lower optical losses of the $n\lambda/4$ grating-gate waveguide mode, as reflected in the stronger absorption minima in the TDS plots of Figure 2.

Consistently, a similar behavior is also predicted for increasing E_F. The simulations indicate a weak gate-tuning of the total GDD, for the same E_F (100–300 meV) used to describe the gate modulation of the reflectance (Figure 2). As a consequence of the higher modulator GDD, the compensation of the total GDD over the whole QCL band becomes less effective.

To explore the efficacy of the coupled cavity configuration in modifying the intracavity QCL mode dynamics, we trace the QCL intermode beatnote map by employing the set-up in **Figure 5**a.

The comparison between the CW emission spectra of the bare laser (Figure 5b) and the modulator-coupled QCL (Figure 5c) does not show significant differences in mode distribution, spacing, spectral coverage, and relative intensities.

The electrical intermode beatnote maps measured in the QCL coupled with each of the three SLG modulators with different p
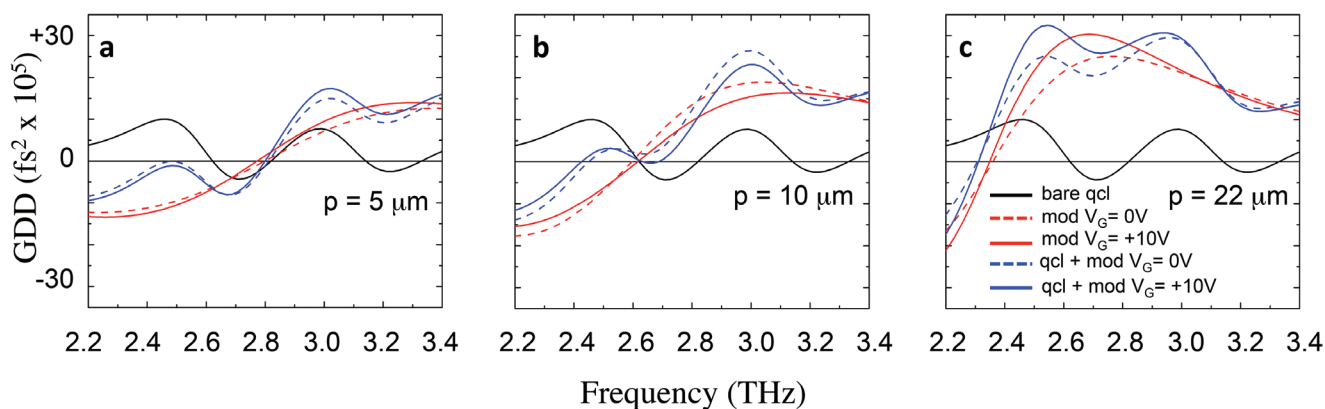
ADVANCED
SCIENCE NEWS
www.advancedsciencenews.com

ADVANCED
FUNCTIONAL
MATERIALS
www.afm-journal.de

Figure 4. GDD of QCL-modulator integrated system: a–c) GDD of heterogeneous QCL frequency comb calculated as a function of frequency when the QCL is uncoupled (black), or coupled with the SLG modulator (blue), and of standalone SLG modulator (red), at $V_G = 0V$ (continuous line) and $V_G = +10V$ (dashed line), for $p = 5\ \mu m$ (a); $p = 10\ \mu m$ (b); and $p = 22\ \mu m$ (c).
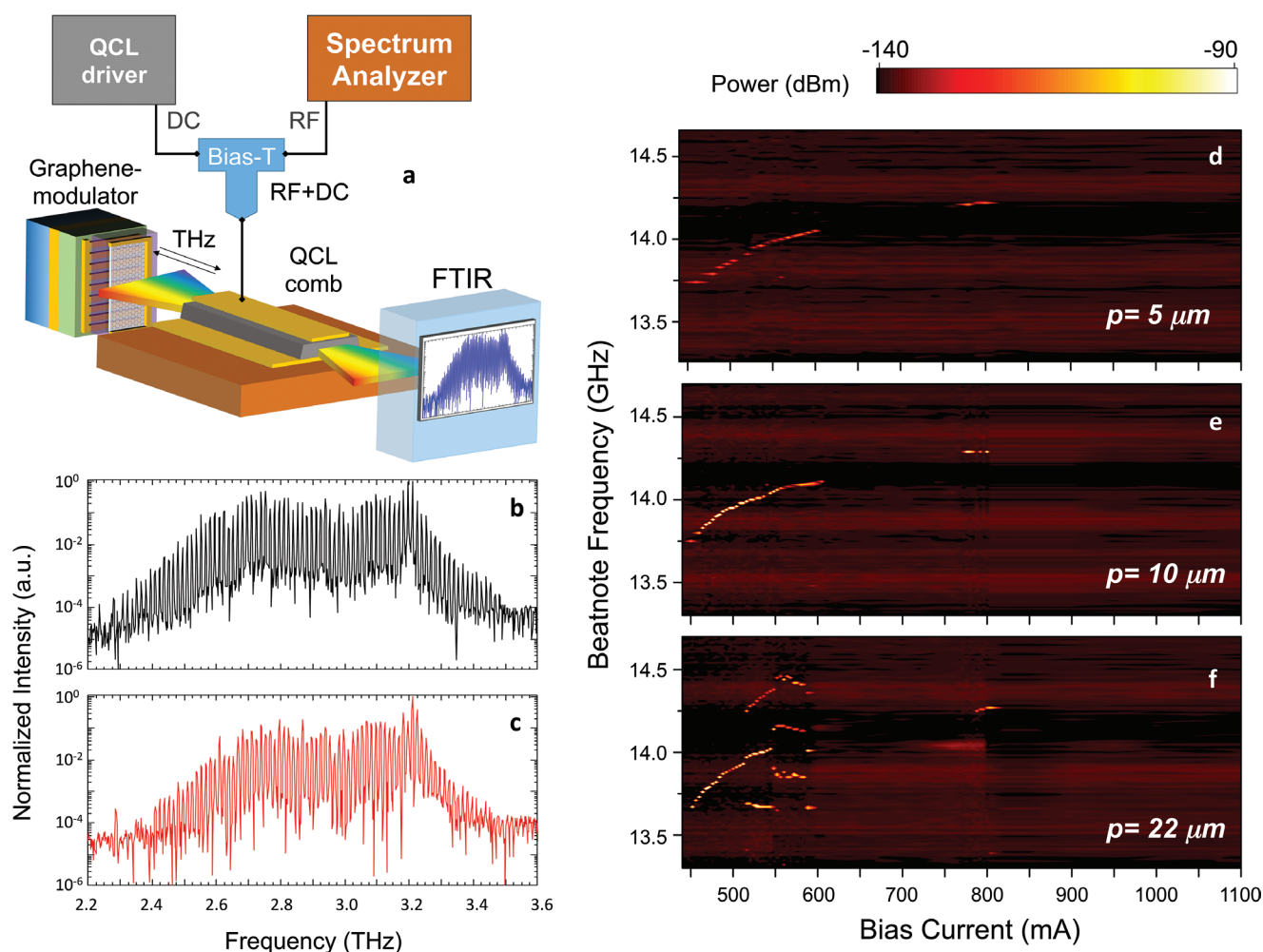

Figure 5. QCL frequency comb embedding a SLG modulator: a) Schematic experimental set-up. The SLG modulator is positioned on a moving piezoelectric stage in close proximity (50 µm) to the back facet of a multimode heterogeneous THz QCL. The modulator is coupled on the same Cu mount with the QCL onto the cold-head of a He-flow cryostat. In this configuration, the back-reflected radiation is injected into the QCL wave-guide, while the emission from the front facet is collected into a Fourier-Transform InfraRed (FTIR) spectrometer. The intermode beatnote maps are recorded with a radio frequency (RF) spectrum analyzer (Rohde & Schwarz FSW). b,c) FTIR emission spectra at 15 K, under vacuum, with ~0.075 cm^{-1} resolution, whilst driving the QCL in CW with 780 mA from bare QCL (b) and QCL-modulator tightly coupled system (c), for $p = 10\ \mu m$ at $V_G = 0V$. d–f) Intermode beatnote maps as a function of CW driving current at 15 K in the QCL-modulator system with $p = 5\ \mu m$ (d), $p = 10\ \mu m$ (e), $p = 22\ \mu m$ (f). The beatnote signal is extracted from the bias line using a bias-tee with a RF spectrum analyzer, and is recorded with resolution bandwidth (RBW): 500 Hz, video bandwidth (VBW): 500 Hz, sweep time (SWT): 20 ms, root mean square (RMS) acquisition mode.
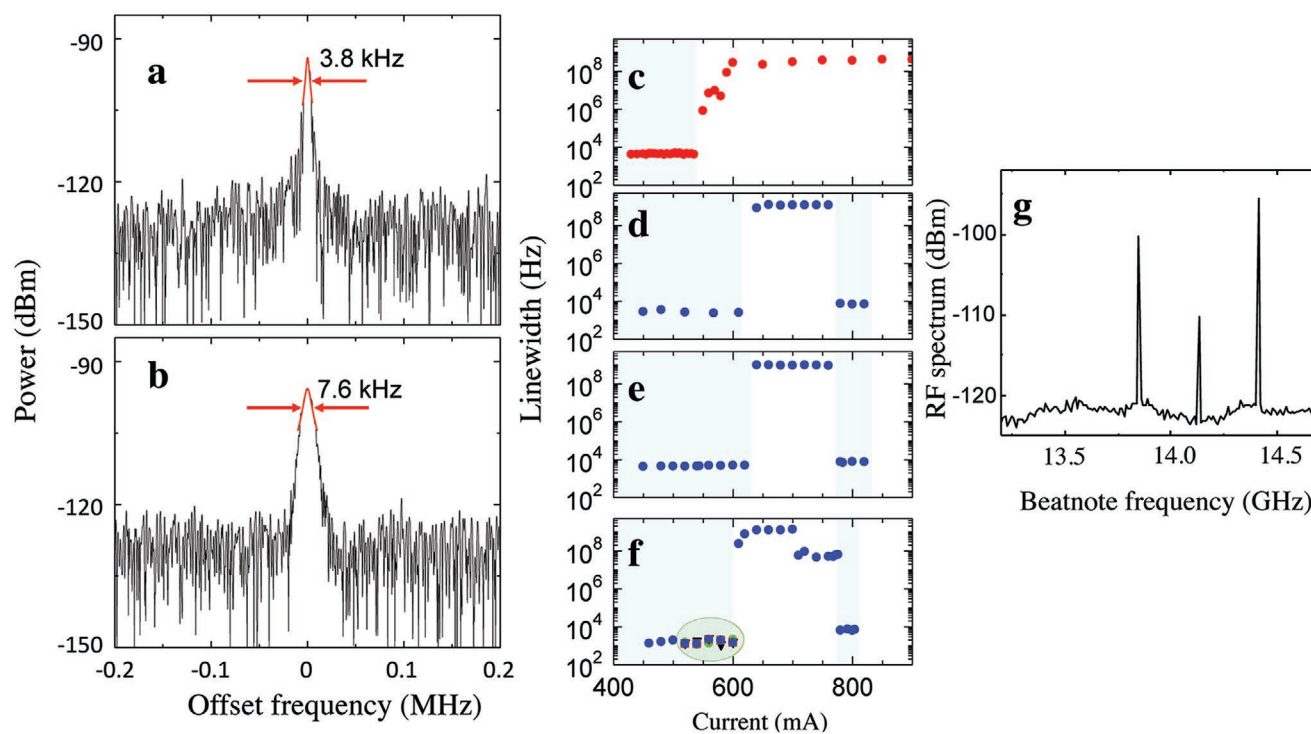
ADVANCED
SCIENCE NEWS
www.advancedsciencenews.com

ADVANCED
FUNCTIONAL
MATERIALS
www.afm-journal.de

Figure 6. Analysis of the intermode beatnote linewidths. a,b) Intermode beatnote signal from QCL integrated with SLG modulator with $p = 10$ μm at 500 (a) and 800 mA (b), measured in CW, at 15 K. The RF spectrum analyzer settings are: RWB: 10 kHz, VBW: 100 kHz, SWT: 200 ms, RMS acquisition mode. c–f) Evolution of the intermode beatnote linewidths as a function of QCL driving current for bare-cavity QCL[46] (c), or when the QCL is coupled with the SLG modulators with $p = 5$ μm (d); $p = 10$ μm (e); and $p = 22$ μm (f). The red and green marks in (f), identified via the green shaded ellipse, correspond to the linewidths of the multiple beatnotes shown in (g). g) Intermode beatnote signal acquired from QCL integrated with SLG modulator with $p = 22$ μm at 560 mA. The light blue shaded areas identify the region in which the laser behaves as a stable frequency comb synthesizer.

(Figure 5d–f), show changes in the intracavity dynamic range, when compared with the corresponding maps measured on the bare QCL[54] (Figure S8, Supporting Information), or with that collected coupling the same laser with an Au mirror placed at the same distance.[58] Furthermore, the different p and related reflectance spectra affect the QCL intracavity mode dynamics. Coupling the QCL with SLG modulators with $p = 5$ and 10 μm (Figure 5d,e), we first observe a region of single and narrow (3.8 kHz, **Figure 6**a) beatnote extending over a continuous current range ~165 mA (440–605 mA), significantly larger than that of the corresponding bare QCL (106 mA).[54] At larger currents (605–760 mA) we observe, in both cases (Figure 5d,e), a broad beatnote characteristic of a lasing regime in which the group velocity dispersion is large enough to prevent locking of the lasing modes in frequency and phase, simultaneously, via FWM.

On the other hand, when coupling the QCL with a $p = 22$ μm modulator, a single and narrow beatnote appears only in a very restricted operational range (440–520 mA), comparable with that observed in the bare QCL.[54] Differently from the bare QCL,[54] at higher currents (520–600 mA), the device shows a region of three narrow beatnotes. In the bare laser, we first observe multiple beatnotes, indicating lasing from higher order lateral modes, then a single beatnote and, finally, double beatnotes, reflecting the dual comb behavior of the laser.[54] Conversely, in Figure 5f, multiple beatnotes persist from 520 to 600 mA unveiling complex intracavity dynamics[67] and

the lack of GDD compensation, as predicted by simulations (Figure 4c). The tuning coefficients of the three beatnotes in the 515–558 mA and 558–600 mA ranges are dissimilar, indicating that, while in the first portion of the dynamic range the three active regions embedded in the QCL core are individually behaving like frequency combs, in the second current range, higher order lateral modes can interfere with the main QCL modes, preventing comb operation.[68]

In all cases (Figure 5d–f) the beatnote turns again single and narrow (7.6 kHz, Figure 6b) at larger driving currents in the range 760–820 mA, when coupling the QCL with SLG modulators with $p = 5$, 10 μm, and over a slightly narrower range (780–820 mA) when $p = 22$ μm. In this new operating regime, not observed either in the bare-QCL frequency comb,[54] or while coupling the same QCL with an Au mirror,[58] we retrieve a stable, high-intensity (30 dBm), narrow (5–7 kHz) single beatnote, with an emission spectrum covering a 1.2 THz bandwidth (Figure 5c), with 98 equidistant optical modes. The coupling with the SLG modulators results in a stable frequency comb operation through 35% of the laser operational range, as extracted from the data of Figures 5e and 6e, much larger than reported in previous passive THz QCL frequency combs,[53,54] to the best of our knowledge. Such an effect is almost independent of V_G, as can be seen by plotting the intermode beatnote linewidths for different V_G with $p = 10$ μm (see Supporting Information). The beatnote map and QCL emission spectra remain almost the same.

The evolution of the emission spectra measured in the bare heterogeneous QCL[54] shows that the three active regions each possess slightly different threshold current densities,[65] and that the active region reaching threshold at larger bias is that centered at the lowest frequency (2.5 THz). This matches the spectral region in which the modulator-QCL GDD compensation is more effective (Figure 4a–c). Therefore, the appearance of the single beatnote regime at the higher bias is likely the result of dispersion compensation, simultaneously preventing higher-order lateral modes reaching threshold, and locking in phase the family of modes arising from the active region module centered at lower frequency (2.5 THz).

We exclude that phase chirping upon modulation induces a significant effect on the cavity dispersion of our heterogeneous THz QCL since the modulator is not inducing any detectable phase modulation in the QCL.

The analysis of the intermode beatnote linewidth (Figure 6c–f) shows that, at driving currents ≤605 mA, the intermode beatnotes linewidth values are comparable (3–5 kHz, Figure 6d–f) with those measured on the bare laser (Figure 6c), and become slightly narrower (1.5 kHz) when the QCL is coupled with the $p = 22$ μm modulator. Such a linewidth narrowing applies to each individual multiple beatnote (Figure 6g), as an effect of their individual behavior as homogenous QCL frequency comb.[69]

In the 780–820 mA range, the beatnote linewidths becomes larger and range between 6 and 8 kHz, as an effect of the jittering induced by the partial increase of the lattice temperature during CW operation.[54]

In the 605–780 mA range, as in the case of the bare-laser cavity, we retrieve the typical very high phase noise (beatnote linewidths ~10^8–10^9 Hz, as fitted the spectrum analyzer signal with a Lorentzian[50,51,53,54,56,58]) resulting from the GDD-induced entanglement of dispersion.

3. Conclusions

We demonstrated a modulator design, comprising a grating-gated graphene capacitor on a polyimide quarter wave resonant cavity. This ensures frequency scaling by-design, and efficient (90%) amplitude modulation at high speeds (>20 kHz). It can be extended to alternative photonic concepts, such as spatial light modulators or nano switches. The ease of implementation and flexible design enables integration with existing laser sources, so to alter their intracavity field and mode dynamics. The stable frequency comb operation, close to the laser peak power, and over a dynamic range 35% of the laser operational regime, much wider than other passive approaches,[42–46] proves the versatility of our modulator. Our integrated graphene modulator-QCL has a potential for high-resolution and high-precision spectroscopy,[68] and quantum metrology.[68,70] It could be integrated in a compact, Peltier-cooled portable configuration, which can operate at 250 K.[71] A miniaturized frequency comb delivering >1 mW optical powers, with >90 equidistant modes, tunable over 35% of the operational range, can allow applications not addressed thus far, such as manipulation of cold atoms and molecules, sensing in space science, and entanglement of the QCL optical modes, crucial for one-way quantum computing.

4. Experimental Section

Device Fabrication: To fabricate the grating-gated SLG THz modulators, we first spin-coat a 14-μm thick polyimide layer on an Au(300 nm)/SiO$_2$(350 nm)/Si back-mirror and bake it at 350 °C for 30 min. We then prepare a metal grating on polyimide layer and deposit 100 nm AlO$_x$ by sputtering and 40 nm HfO$_2$ by atomic layer deposition.

SLG is then grown in a hot wall chemical vapor deposition system on Cu foil (35 μm, Graphene Platform). The foil is loaded into a quartz chamber in a horizontal furnace and the system is evacuated to ~10 mTorr base pressure. 40 sccm H$_2$ is then introduced to attain 400 mTorr and the growth chamber is heated to 1000 °C. The Cu foil is annealed in the same conditions for 30 min. To initiate the growth of SLG, 5 sccm CH$_4$ is used. The growth is terminated after 30 min by turning off all the gases and the heater. The system is naturally cooled down to room temperature. SLG is then placed on AlO$_x$/HfO$_2$ using wet transfer.[31,36] Polymethyl methacrylate (PMMA, A4 950, MicroChem) is spin-coated onto the SLG/Cu foil at 3000 rpm for 60 s and baked at 120 °C for 5 min. The PMMA/SLG/Cu stack is then floated on a solution of 0.1 M Ammonium persulfate (APS) overnight to etch the Cu foil, and then moved in DI water to clean APS residues. The floating PMMA/SLG stack is transferred on AlO$_x$/HfO$_2$/polyimide/Au/SiO$_2$/Si, Figure 1a. The sample is dried in ambient for 2 h and subsequently baked at 120 °C for 15 min. PMMA is removed in acetone and isopropanol (IPA). 5/100 nm Cr/Au are deposited by thermal evaporation for both metal grating gate and contact. Metal gratings with $p = 5, 10, 22, 45$ μm are fabricated with a 50% geometrical fill factor (i.e., the metal width equals the metal gap in the unit cell). As grown and transferred SLG samples are characterized by Raman spectroscopy using a Renishaw InVia spectrometer (Supporting Information).

Full-Wave Electromagnetic Simulations: The complex reflection coefficient and total field distribution under single-frequency illumination of the devices are calculated using the finite element method software COMSOL Multiphysics in the frequency domain. SLG is simulated as a monolayer (0.34 nm) with intraband Drude-like conductivity. The polyimide's (Kapton) optical constants in the THz range are taken from ref. [60], while Au is modeled as a perfect electric conductor. The structures are illuminated with single frequency light, using a port boundary condition, and the amplitude and phase of the reflection coefficient are extracted from the simulation. The resulting GDD is calculated via the second derivative of the phase of the reflection coefficients. The GDD of the bare laser is calculated as in ref. [58].

Modulation Speed: We measure the modulation speed from a self-mixing (SM) experiment, Figure 3c. The self-mixing signal is the down-converted signal associated with the cavity optical feedback experienced by the QCL, once positioned inside an external cavity, comprising the modulator placed at one vertex of the QCL beam path. The modulator is driven by a voltage oscillating at the AM frequency generated by a pulsed driver (Agilent 8114A). The self-mixing signal is then recorded using a lock-in amplifier (Zurich Instruments UHFLI). A single-plasmon CW QCL single mode emission at 2.68 THz is then coupled with the $p = 10$ μm modulator. The modulator driving gate AC voltage is a square-wave signal with amplitude 4.4 V, baseline 0 V, duty cycle 50%, and frequency varying from 10^2 to 10^6 Hz. For an accurate estimate of the reflectance R, we extract the reference level by the self-mixing signal recorded with a moving Au mirror, oscillating at the same frequency. The reference self-mixing signal is almost flat in the frequency range covered in our experiments.

Modulator-Quantum Cascade Laser Integration: The grating-gated SLG THz modulator is integrated with the THz QCL into an external etalon-like configuration, defining a GTI (Figure 5a). The QCL is a 2.9-mm-long, 85-μm-wide Fabry–Pérot laser bar operating as a frequency comb synthesizer in CW over 15% of its operational range. The QCL is mounted on a Cu bar in thermal contact with the cold-finger of liquid-He cryostat, with one of the two emitting facets positioned at the vertex of the input optical path of a vacuum FTIR spectrometer (Bruker vertex 80), for the simultaneous collection of the QCL emission spectra. FTIR spectra are collected in rapid-scan mode, under vacuum, with a 0.075 cm^{-1} resolution, at 15 K. The SLG modulator is integrated with the

QCL inside the cryostat with the help of a piezoelectric stage, enabling tight coupling of the modulator active area with the QCL facet, at 50 µm distance. The intermode beatnote map is acquired as a function of laser drive current at a heat sink temperature of 15 K. The beatnote signal is extracted from the bias line using a bias-tee, and recorded with a RF spectrum analyzer (Rohde & Schwarz FSW; resolution bandwidth: 500 Hz; video bandwidth: 500 Hz; sweep time: 20 ms; RMS acquisition mode).

Supporting Information

Supporting Information is available from the Wiley Online Library or from the author.

Acknowledgements

Conflict of Interest

The authors declare no conflict of interest.

Keywords

[1] S. S. Dhillon, M. S. Vitiello, E. H. Linfield, A. G. Davies, M. C. Hoffmann, J. Booske, C. Paoloni, M. Gensch, P. Weightman, G. P. Williams, E. Castro-Camus, D. R. S. Cumming, F. Simoens, I. Escorcia-Carranza, J. Grant, S. Lucyszyn, M. Kuwata-Gonokami, K. Konishi, M. Koch, C. A. Schmuttenmaer, T. L. Cocker, R. Huber, A. G. Markelz, Z. D. Taylor, V. P. Wallace, J. Axel Zeitler, J. Sibik, T. M. Korter, B. Ellison, S. Rea, et al., *J. Phys. D: Appl. Phys.* **2017**, *50*, 043001.

[2] S. Koenig, D. Lopez-Diaz, J. Antes, F. Boes, R. Henneberger, A. Leuther, A. Tessmann, R. Schmogrow, D. Hillerkuss, R. Palmer, T. Zwick, C. Koos, W. Freude, O. Ambacher, J. Leuthold, I. Kallfass, *Nat. Photonics* **2013**, *7*, 977.

[3] D. M. Mittleman, *Opt. Express* **2018**, *26*, 9417.

[4] A. J. Seeds, H. Shams, M. J. Fice, C. C. Renaud, *J. Lightwave Technol.* **2015**, *33*, 579.

[5] N. Kakenov, M. S. Ergoktas, O. Balci, C. Kocabas, *2D. Mater.* **2018**, *5*, 035018.

[6] R. Köhler, A. Tredicucci, F. Beltram, H. E. Beere, E. H. Linfield, A. G. Davies, D. A. Ritchie, R. C. Iotti, F. Rossi, *Nature* **2002**, *417*, 156.

[7] M. S. Vitiello, G. Scalari, B. Williams, P. De Natale, *Opt. Express* **2015**, *23*, 5167.

[8] A. Dunn, C. Poyser, P. Dean, A. Demić, A. Valavanis, D. Indjin, M. Salih, I. Kundu, L. Li, A. Akimov, A. G. Davies, E. Linfield, J. Cunningham, A. Kent, *Nat. Commun.* **2020**, *11*, 835.

[9] R. Paiella, R. Martini, F. Capasso, C. Gmachl, H. Y. Hwang, D. L. Sivco, J. N. Baillargeon, A. Y. Cho, E. A. Whittaker, H. C. Liu, *Appl. Phys. Lett.* **2001**, *79*, 2526.

[10] S. Barbieri, W. Maineult, S. S. Dhillon, C. Sirtori, J. Alton, N. Breuil, H. E. Beere, D. A. Ritchie, *Appl. Phys. Lett.* **2007**, *91*, 143510.

[11] P. Gellie, S. Barbieri, J.-F. Lampin, P. Filloux, C. Manquest, C. Sirtori, I. Sagnes, S. P. Khanna, E. H. Linfield, A. G. Davies, H. Beere, D. Ritchie, *Opt. Express* **2010**, *18*, 20799.

[12] M. A. Belkin, F. Capasso, *Phys. Scr.* **2015**, *90*, 118002.

[13] M. A. Kainz, M. P. Semtsiv, G. Tsianos, S. Kurlov, W. T. Masselink, S. Schönhuber, H. Detz, W. Schrenk, K. Unterrainer, G. Strasser, A. M. Andrews, *Opt. Express* **2019**, *27*, 20688.

[14] L. Bosco, M. Franckié, G. Scalari, M. Beck, A. Wacker, J. Faist, *Appl. Phys. Lett.* **2019**, *115*, 010601.

[15] F. Castellano, L. Li, E. H. Linfield, A. G. Davies, M. S. Vitiello, M. S. Vitiello, *Sci. Rep.* **2016**, *6*, 23053.

[16] A. Tredicucci, M. S. Vitiello, *IEEE. J. Sel. Top. Quantum Electron.* **2014**, *20*, 130.

[17] M. Romagnoli, V. Sorianello, M. Midrio, F. H. L. Koppens, C. Huyghebaert, D. Neumaier, P. Galli, W. Templ, A. D'errico, A. C. Ferrari, *Nat. Rev. Mater.* **2018**, *3*, 392.

[18] V. Sorianello, M. Midrio, G. Contestabile, I. Asselberghs, J. Van Campenhout, C. Huyghebaert, I. Goykhman, A. K. Ott, A. C. Ferrari, M. Romagnoli, *Nat. Photonics* **2018**, *12*, 40.

[19] M. Liu, X. Yin, E. Ulin-Avila, B. Geng, T. Zentgraf, L. Ju, F. Wang, X. Zhang, *Nature* **2011**, *474*, 64.

[20] R. R. Nair, P. Blake, A. N. Grigorenko, K. S. Novoselov, T. J. Booth, T. Stauber, N. M. R. Peres, A. K. Geim, *Science* **2008**, *320*, 1308.

[21] T. Stauber, N. M. R. Peres, A. K. Geim, *Phys. Rev. B* **2008**, *78*, 085432.

[22] M. Liu, X. Yin, X. Zhang, *Nano Lett.* **2012**, *12*, 1482.

[23] C. Backes, A. M. Abdelkader, C. Alonso, A. Andrieux-Ledier, R. Arenal, J. Azpeitia, N. Balakrishnan, L. Banszerus, J. Barjon, R. Bartali, S. Bellani, C. Berger, R. Berger, M. M. B. Ortega, C. Bernard, P. H. Beton, A. Beyer, A. Bianco, P. Bøggild, F. Bonaccorso, G. B. Barin, C. Botas, R. A. Bueno, D. Carriazo, A. Castellanos-Gomez, M. Christian, A. Ciesielski, T. Ciuk, M. T. Cole, J. Coleman, et al., *2D. Mater.* **2020**, *7*, 022001.

[24] K. F. Mak, L. Ju, F. Wang, T. F. Heinz, *Solid State Commun.* **2012**, *152*, 1341.

[25] L. M. Malard, K. Fai Mak, A. H. Castro Neto, N. M. R. Peres, T. F. Heinz, *New J. Phys.* **2013**, *15*, 015009.

[26] V. P. Gusynin, S. G. Sharapov, J. P. Carbotte, *New J. Phys.* **2009**, *11*, 095013.

[27] J. Horng, C.-F. Chen, B. Geng, C. Girit, Y. Zhang, Z. Hao, H. A. Bechtel, M. Martin, A. Zettl, M. F. Crommie, Y. R. Shen, F. Wang, *Phys. Rev. B* **2011**, *83*, 165113.

[28] K. F. Mak, M. Y. Sfeir, Y. Wu, C. H. Lui, J. A. Misewich, T. F. Heinz, *Phys. Rev. Lett.* **2008**, *101*, 196405.

[29] K. Fan, W. J. Padilla, *Mater. Today* **2015**, *18*, 39.

[30] P. H. Q. Pham, W. Zhang, N. V. Quach, J. Li, W. Zhou, D. Scarmardo, E. R. Brown, P. J. Burke, *Nat. Commun.* **2017**, *8*, 2233.

[31] A. C. Ferrari, F. Bonaccorso, V. Fal'ko, K. S. Novoselov, S. Roche, P. Bøggild, S. Borini, F. H. L. Koppens, V. Palermo, N. Pugno, J. A. Garrido, R. Sordan, A. Bianco, L. Ballerini, M. Prato, E. Lidorikis, J. Kivioja, C. Marinelli, T. Ryhänen, A. Morpurgo, J. N. Coleman, V. Nicolosi, L. Colombo, A. Fert, M. Garcia-Hernandez, A. Bachtold, G. F. Schneider, F. Guinea, C. Dekker, M. Barbone, et al., *Nanoscale* **2015**, *7*, 4598.

[32] O. Balci, E. O. Polat, N. Kakenov, C. Kocabas, *Nat. Commun.* **2015**, *6*, 6628.

[33] M. Tamagnone, S. Capdevila, A. Lombardo, J. Wu, A. Centeno, A. Zurutuza, A. Ionescu, A. C. Ferrari, J. R. Mosig, arXiv:1806.02202, **2018**.

[34] F. Bonaccorso, Z. Sun, T. Hasan, A. C. Ferrari, *Nat. Photonics* **2010**, *4*, 611.

[35] C. T. Phare, Y.-H. Daniel Lee, J. Cardenas, M. Lipson, *Nat. Photonics* **2015**, *9*, 511.

[36] F. Bonaccorso, A. Lombardo, T. Hasan, Z. Sun, L. Colombo, A. C. Ferrari, *Mater. Today* **2012**, *15*, 564.

[37] B. Sensale-Rodriguez, R. Yan, S. Rafique, M. Zhu, W. Li, X. Liang, D. Gundlach, V. Protasenko, M. M. Kelly, D. Jena, L. Liu, H. G. Xing, *Nano Lett.* **2012**, *12*, 4518.

[38] G. Liang, X. Hu, X. Yu, Y. Shen, L. H. Li, A. G. Davies, E. H. Linfield, H. K. Liang, Y. Zhang, S. F. Yu, Q. J. Wang, *ACS Photonics* **2015**, *2*, 1559.

[39] Y. Cao, S. Gan, Z. Geng, J. Liu, Y. Yang, Q. Bao, H. Chen, *Sci. Rep.* **2016**, *6*, 22899.

[40] P. Weis, J. L. Garcia-Pomar, M. Höh, B. Reinhard, A. Brodyanski, M. Rahm, *ACS Nano* **2012**, *6*, 9118.

[41] D. Shrekenhamer, S. Rout, A. C. Strikwerda, C. Bingham, R. D. Averitt, S. Sonkusale, W. J. Padilla, *Opt. Express* **2011**, *19*, 9968.

[42] S. H. Lee, M. Choi, T.-T. Kim, S. Lee, M. Liu, X. Yin, H. K. Choi, S. S. Lee, C.-G. Choi, S.-Y. Choi, X. Zhang, B. Min, *Nat. Mater.* **2012**, *11*, 936.

[43] P. Q. Liu, I. J. Luxmoore, S. A. Mikhailov, N. A. Savostianova, F. Valmorra, J. Faist, G. R. Nash, *Nat. Commun.* **2015**, *6*, 8969.

[44] Z. Chen, X. Chen, Li Tao, K. Chen, M. Long, X. Liu, K. Yan, R. I. Stantchev, E. Pickwell-Macpherson, J.-B. Xu, *Nat. Commun.* **2018**, *9*, 4909.

[45] T. T. Kim, S. S. Oh, H. D. Kim, H. S. Park, O. Hess, B. Min, S. Zhang, *Sci. Adv.* **2017**, *3*, 1701377.

[46] J. Zhou, D. R. Chowdhury, R. Zhao, A. K. Azad, H.-T. Chen, C. M. Soukoulis, A. J. Taylor, J. F. O'hara, *Phys. Rev. B* **2012**, *86*, 035448.

[47] Z. Sun, A. Martinez, F. Wang, *Nat. Photonics* **2016**, *10*, 227.

[48] P. Gopalan, B. Sensale-Rodriguez, *Adv. Opt. Mater.* **2020**, *8*, 1900550.

[49] A. Hugi, G. Villares, S. Blaser, H. C. Liu, J. Faist, *Nature* **2012**, *492*, 229.

[50] D. Burghoff, T.-Y. Kao, N. Han, C. W. I. Chan, X. Cai, Y. Yang, D. J. Hayton, J.-R. Gao, J. L. Reno, Q. Hu, *Nat. Photonics* **2014**, *8*, 462.

[51] M. Rösch, G. Scalari, M. Beck, J. Faist, *Nat. Photonics* **2015**, *9*, 42.

[52] G. Villares, J. Faist, *Opt. Express* **2015**, *23*, 1651.

[53] M. Rösch, M. Beck, M. J. Süess, D. Bachmann, K. Unterrainer, J. Faist, G. Scalari, *Nanophotonics* **2018**, *7*, 237.

[54] K. Garrasi, F. P. Mezzapesa, L. Salemi, L. Li, L. Consolino, S. Bartalini, P. De Natale, A. G. Davies, E. H. Linfield, M. S. Vitiello, *ACS Photonics* **2019**, *6*, 73.

[55] F. Gires, P. Tournois, *C. R. Acad. Sci.* **1964**, *258*, 6112.

[56] Y. Yang, D. Burghoff, J. Reno, Q. Hu, *Opt. Lett.* **2017**, *42*, 3888.

[57] F. Wang, H. Nong, T. Fobbe, V. Pistore, S. Houver, S. Markmann, N. Jukam, M. Amanti, C. Sirtori, S. Moumdji, R. Colombelli, L. Li, E. Linfield, G. Davies, J. Mangeney, J. Tignon, S. Dhillon, *Laser Photonics Rev.* **2017**, *11*, 1770042.

[58] F. P. Mezzapesa, V. Pistore, K. Garrasi, L. Li, A. G. Davies, E. H. Linfield, S. Dhillon, M. S. Vitiello, *Opt. Express* **2019**, *27*, 20231.

[59] J. Hillbrand, P. Jouy, M. Beck, J. Faist, *Opt. Lett.* **2018**, *43*, 1746.

[60] P. D. Cunningham, N. N. Valdes, F. A. Vallejo, L. M. Hayden, B. Polishak, X.-H. Zhou, J. Luo, A. K.-Y. Jen, J. C. Williams, R. J. Twieg, *J. Appl. Phys.* **2011**, *109*, 043505.

[61] T. J. Echtermeyer, L. Britnell, P. K. Jasnos, A. Lombardo, R. V. Gorbachev, A. N. Grigorenko, A. K. Geim, A. C. Ferrari, K. S. Novoselov, *Nat. Commun.* **2011**, *2*, 458.

[62] P. Dean, Y. Leng Lim, A. Valavanis, R. Kliese, M. Nikolić, S. P. Khanna, M. Lachab, D. Indjin, Z. Ikonić, P. Harrison, A. D. Rakić, E. H. Linfield, A. G. Davies, *Opt. Lett.* **2011**, *36*, 2587.

[63] T. Taimre, M. Nikolić, K. Bertling, Y. L. Lim, T. Bosch, A. D. Rakić, *Adv. Opt. Photonics* **2015**, *7*, 570.

[64] F. P. Mezzapesa, L. L. Columbo, M. Brambilla, M. Dabbicco, S. Borri, M. S. Vitiello, H. E. Beere, D. A. Ritchie, G. Scamarcio, *Opt. Express* **2013**, *21*, 13748.

[65] L. H. Li, K. Garrasi, I. Kundu, Y. J. Han, M. Salih, M. S. Vitiello, A. G. Davies, E. H. Linfield, *Electron. Lett.* **2018**, *54*, 1229.

[66] H. Li, M. Yan, W. Wan, T. Zhou, K. Zhou, Z. Li, J. Cao, Q. Yu, K. Zhang, M. Li, J. Nan, B. He, H. Zeng, *Adv. Sci.* **2019**, *6*, 1900460.

[67] H. Li, P. Laffaille, D. Gacemi, M. Apfel, C. Sirtori, J. Leonardon, G. Santarelli, M. Rösch, G. Scalari, M. Beck, J. Faist, W. Hänsel, R. Holzwarth, S. Barbieri, *Opt. Express* **2015**, *23*, 33270.

[68] L. Consolino, M. Nafa, F. De Regis, F. Cappelli, K. Garrasi, F. P. Mezzapesa, L. Li, A. G. Davies, E. H. Linfield, M. S. Vitiello, S. Bartalini, P. De Natale, *Commun. Phys.* **2020**, *3*, 69.

[69] A. Di Gaspare, L. Viti, H. E. Beere, D. D. Ritchie, M. S. Vitiello, *Nanophotonics* **2020**, https://doi.org/10.1515/nanoph-2020-0378.

[70] L. Consolino, M. Nafa, F. Cappelli, K. Garrasi, F. P. Mezzapesa, L. Li, A. G. Davies, E. H. Linfield, M. S. Vitiello, P. De Natale, S. Bartalini, *Nat. Commun.* **2019**, *10*, 2938.

[71] A. Khalatpour, A. K. Paulsen, C. Deimert, Z. R. Wasilewski, Q. Hu, *Nat. Photonics* **2020**, https://doi.org/10.1038/s41566-020-00707-5.